



Solar Wind Density and Core Temperature Derived from the PSP Quasi-thermal Noise Measurements

Xianming Zheng¹ , Kaijun Liu¹ , Mihailo M. Martinović^{2,3} , Viviane Pierrard^{4,5} , Mingzhe Liu^{3,6} , Qingbao He¹ ,
Kun Cheng¹ , Yuqi Liu¹, and Yan Wang¹

¹Department of Earth and Space Sciences, Southern University of Science and Technology, Shenzhen, People's Republic of China; liukj@sustech.edu.cn

²Lunar and Planetary Laboratory, University of Arizona, Tucson, AZ, USA; mmartinovic@arizona.edu

³LESIA, Observatoire de Paris, Meudon, France

⁴Royal Belgian Institute for Space Aeronomy (BIRA-IASB), Space Physics, Solar-Terrestrial Center of Excellence, Brussels, Belgium

⁵Center for Space Radiation (CSR), Georges Lemaître Centre for Earth and Climate Research (TECLIM), Earth and Life Institute—Climate Sciences (ELI-C), Université Catholique de Louvain, Louvain-la-Neuve, Belgium

⁶Space Sciences Laboratory, University of California, Berkeley, CA 94720-7450, USA

Received 2023 December 5; revised 2024 January 25; accepted 2024 January 26; published 2024 March 8

Abstract

Quasi-thermal noise (QTN) spectroscopy is a valuable method to deduce important parameters in space plasma, such as plasma density and temperature, especially when direct particle measurements are not available. The present study develops a new fitting method to fit the QTN spectra observed by the Parker Solar Probe (PSP) with a comprehensive theoretical QTN spectral model. By combining the steepest descent and Levenberg–Marquardt algorithms, the new method is more flexible with initial guess values but still yields reliable solar wind electron density and temperature values. The new method is applied to derive the solar wind density and core temperature from the QTN measurements during 10 encounters of PSP. The electron density and temperature values obtained vary with the radial distance from the Sun as $n_e \propto r^{-2.12}$ and $T_e \propto r^{-0.71}$, both of which are consistent with existing models and previous results.

Unified Astronomy Thesaurus concepts: Solar wind (1534); Space probes (1545); Space plasmas (1544); Plasma physics (2089)

1. Introduction

Quasi-thermal noise (QTN) spectroscopy provides a valuable method to obtain plasma density and temperature information, especially when direct measurements are not available. Early theoretical studies have suggested that a QTN spectrum measured by electric field antennas on board a spacecraft in a space plasma depends on the velocity distributions of the plasma particles (Fejer & Kan 1969). Subsequently, plasma parameters, such as density and temperature, can be deduced by fitting the QTN spectra recorded with a theoretical QTN model (Meyer-Vernet et al. 2017). The technique was first used in the ISEE-3 mission (Knoll et al. 1978; Meyer-Vernet 1979) and has also been routinely used to infer in situ electron densities and temperatures in various solar wind missions (e.g., Ulysses, Maksimovic et al. 1995; Issautier et al. 1996, 1999; Martinović et al. 2017; Wind, Maksimovic et al. 1998; Issautier et al. 2005; Martinović et al. 2020, 2022; STEREO, Zouganelis et al. 2010; Martinović et al. 2016) and planetary missions (such as Cassini, Moncuquet et al. 2005).

In theory, a QTN spectrum is determined by both the antenna geometry and the particle (mostly electron) velocity distributions (Couturier et al. 1981; Meyer-Vernet & Perche 1989). The influence of the former is characterized by the antenna response function (ARF), which varies across different missions. About the particle velocity distributions, theoretical QTN spectra have been derived for plasmas with one-Maxwellian, two-Maxwellian, kappa, and flat-top electron

distributions. In the solar wind plasma, the two-Maxwellian distribution composed of the core and halo electrons is often assumed. In the case of a wire dipole antenna with $L_{\text{ant}} > L_D$, where L_{ant} is the antenna length of each wire and L_D is the plasma Debye length, the QTN spectrum derived for the two-Maxwellian electron distribution follows a standard pattern across three distinct frequency (f) regions: a spectral plateau at frequencies below the electron plasma frequency (f_p), a spectral peak just above f_p , and a power-law spectral variation of f^{-3} at $f > f_p$.

The present study analyzes the QTN spectra recorded by the Parker Solar Probe (PSP) to derive the solar wind electron density and temperature. PSP is orbiting the Sun on highly elliptical trajectories (Fox et al. 2016). Its perihelion gradually decreased from $35.7 R_s$ (R_s is the solar radius) to $9.86 R_s$ (estimated for 2024 December), after multiple gravity assists from Venus. The FIELDS instrument on board PSP was designed to measure DC and fluctuation magnetic and electric fields (Bale et al. 2016). It contains two wire dipoles with $L_{\text{ant}} = 2$ m and a 1.98 m gap between the two arms of each dipole. The large gap makes it challenging to fit the observed QTN spectra with theoretical QTN models, as most of the models were derived for the case of dipoles with a negligible gap. Nevertheless, early studies have shown that the solar wind density could be inferred by correlating the peak frequency in a QTN spectrum with f_p (Gurnett 1998; Bale et al. 2019). In addition, as the discrepancies due to the antenna gap primarily appear in the vicinity of the spectral peak around f_p in a QTN spectrum, some studies estimated the electron core temperature T_c (Moncuquet et al. 2020) and total temperature T_e (Maksimovic et al. 2020; Liu et al. 2021) by separately fitting the QTN spectra below or above f_p . Recently, Martinović et al. (2022; hereafter M22) calculated the ARF for PSP using the Analysis of

Wire Antennas and Scatterers (AWAS) software and achieved better agreement between the observed and the model QTN spectra around the spectral peak. The electron density (n_e) and core temperature were then found via standard Levenberg–Marquardt (LM) least square fit of the observed QTN spectra (during Encounter 7) using the new model. While the results of M22 are consistent with the PSP particle measurement and the previous studies, the LM algorithm adopted for inverting plasma parameters suffers from its sensitivity to initial parameter guesses.

Following M22, the present study uses the new ARF to calculate the theoretical QTN spectrum. The QTN measurements during 10 encounters of PSP (Encounters 3 to 13, except Encounter 11) are then fitted to the theoretical QTN spectrum in the frequency range around f_p to derive the solar wind electron density and temperature. A new fitting method has been developed by combining the steepest descent and Levenberg–Marquardt algorithms. The new method, referred to as the “steepest descent and Levenberg–Marquardt” (SL) method in the rest of the paper, is more flexible with initial guess values but still yields reliable solar wind electron density and temperature.

The rest of the paper is organized as follows. Section 2 introduces the PSP QTN measurements and the theoretical QTN model used. Section 3 describes the new SL fitting approach. Section 4 presents the electron density and core temperature calculated and statistically examines their variations with the heliocentric distance. Finally, Section 5 summarizes the study and discusses the limitations and possible future work.

2. PSP QTN Measurements and Theoretical Model

The Radio Frequency Spectrometer (RFS) of FIELDS on board PSP collects the electric field fluctuations up to 19.2 MHz (Pulupa et al. 2017). The QTN measurements analyzed in the present study were made by the Low Frequency Receiver (LFR) of RFS. It covers the frequency range of 10.54 kHz to 1.69 MHz with 64 logarithmically spaced frequencies, providing $\sim 4.5\%$ spectral resolution. As in M22, the present study focuses on the QTN spectra measured when the FIELDS antennas were not biased because the bias current produces an increased impact noise signal just below f_p . The QTN measurements during 10 encounters (Encounter 3 to Encounter 13 except Encounter 11, as Encounter 11 does not contain unbiased intervals) have been analyzed, but only the V1–V2 channel data are considered for simplicity. In addition, the study uses the 1 minute median data in order to remove short-term signal pollution.

The PSP QTN measurements are fitted to the theoretical QTN model of M22 assuming that the solar wind electrons consist of two isotropic Maxwellians: a thermal core and a suprathermal halo. As described in Section 2.2 of M22, the synthetic QTN spectrum generally contains contributions from the electrons, protons, impact (shot) noise, galaxy radiation, and instrument noise. However, around f_p , the synthetic QTN spectrum is dominated by the contribution from the electrons, i.e., the electron QTN. Correspondingly, the present study directly fits the observed QTN spectra in the range of $0.9\text{--}5f_p$ to the theoretical electron QTN. Note that the ARF involved in the calculation of the electron QTN has been accurately determined using the AWAS software for PSP in M22. In addition, the antenna gain factor $\Gamma = 0.33$ has been adopted as in Moncuquet et al. (2020) and Liu et al. (2023).

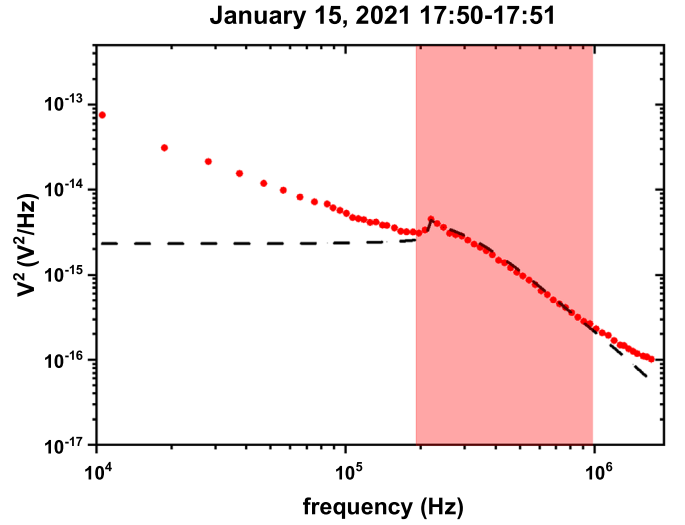


Figure 1. PSP QTN spectrum (1 minute median values) observed by the V1–V2 channel of LFR between 17:50 and 17:51 UT on 2021 January 15 and fitted theoretical electron QTN using the LM method. The dotted and dashed curves display the observed and theoretical QTN spectra, respectively. The red region marks the frequency range of $0.9\text{--}5f_p$, where the observed spectrum is fitted to the theoretical electron QTN model.

3. Steepest Descent and Levenberg–Marquardt Method

In QTN spectroscopy, relevant plasma parameters are determined by minimizing the difference between observed and model QTN spectra. The difference is often quantified as the chi-square: $\chi^2 = \sum_{i=1}^N \frac{(O_i - E_i)^2}{O_i}$, where O_i and E_i are the values of the observed and model QTN spectra, and N is the number of data points. As a widely used optimization algorithm, the LM method was often employed in QTN spectroscopy to find the plasma parameters that minimize χ^2 . The parameter update rule in the LM algorithm is

$$x_{k+1} = x_k - (J_k^T J_k + \lambda I)^{-1} g_k, \quad (1)$$

where the subscripts k and $k+1$ represent the numbers of iteration steps, x represents the parameter vector, J is the Jacobian matrix (the superscript “ T ” denotes its transpose), λ is the LM parameter, I is an identity matrix, and g_k is the gradient of χ^2 (with respect to the parameter vector). In comparison, the update rules in the simpler steepest descent (SD) and Gauss–Newton methods are $x_{k+1} = x_k - \alpha g_k$ and $x_{k+1} = x_k - (J_k^T J_k)^{-1} g_k$, respectively. Here α is a positive step size factor. It is clear from Equation (1) that the LM method falls between the SD method and the Gauss–Newton method. It approaches the SD method when λ is large but reverts to the Gauss–Newton method for small values of λ (Aster et al. 2018).

The LM method was also used in M22 to obtain the solar wind electron parameters by fitting the PSP observed QTN spectra with the improved theoretical QTN model. As an example, the dots in Figure 1 display the PSP QTN spectrum (1 minute median values) observed between 17:50 and 17:51 UT on 2021 January 15. The observed spectrum in the frequency range of $0.9\text{--}5f_p$ (highlighted in red) is fitted to the theoretical electron QTN model of M22 using the LM method, and the fitted model QTN spectrum is shown as the dashed curve. Following M22, the initial parameter guesses are: $n_e = 584.03 \text{ cm}^{-3}$, $T_c = 30.29 \text{ eV}$, the halo-to-core electron density ratio $n_h/n_c = 0.01$, and the halo-to-core electron

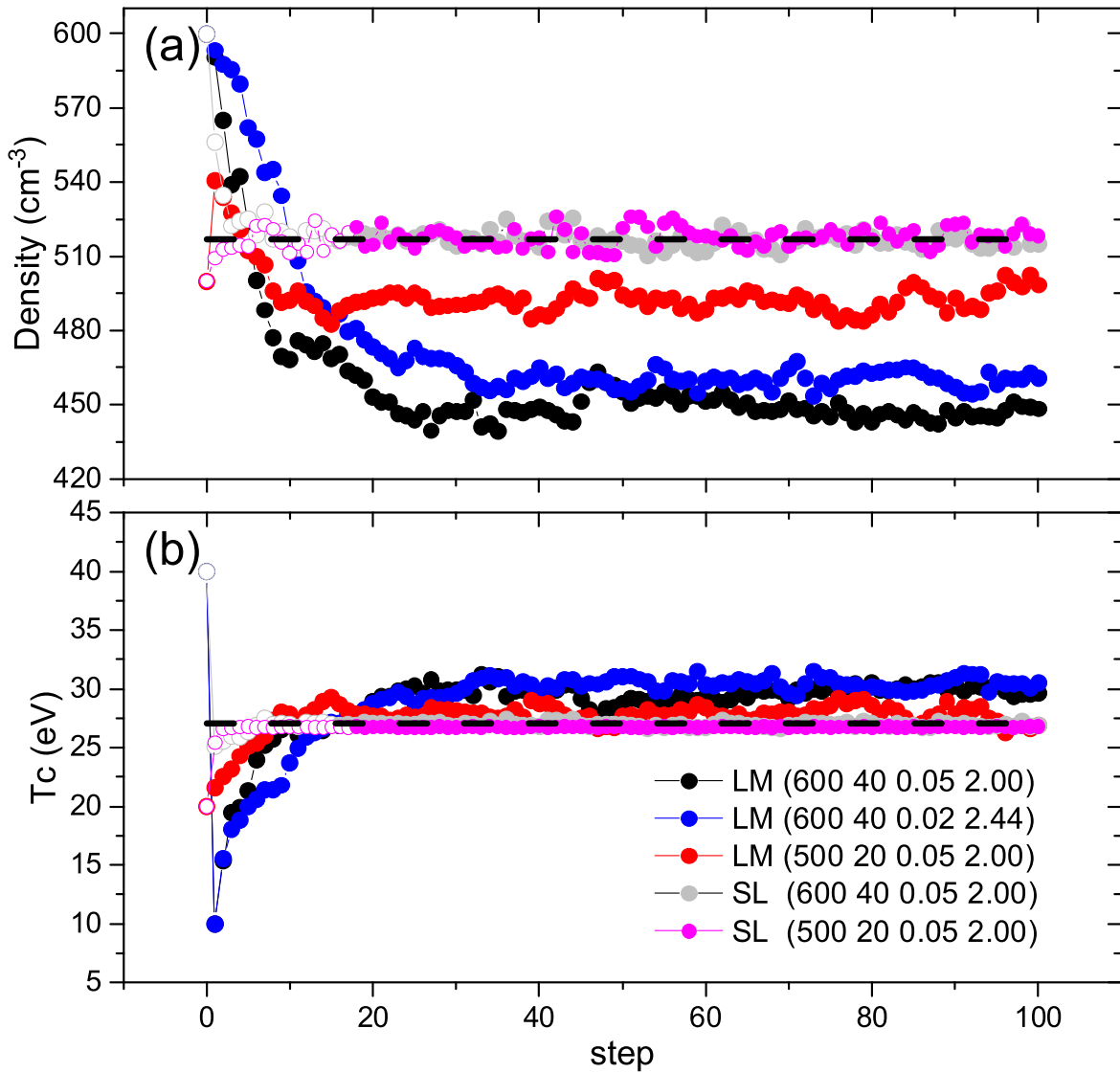


Figure 2. Variations in the obtained (a) electron densities and (b) core temperatures with the number of iteration steps when different initial guess values and fitting methods are used (as labeled in the legend). The horizontal line in each panel marks the “true” value of the corresponding parameter which is given by the LM method using the carefully selected initial guess values (see text for details). For the combined SL method, the results given by the early SD iterations are shown as empty circles to be distinguished from the values yielded by the late LM iterations.

temperature ratio $T_h/T_c = 2.10$. In addition, the LM parameter λ is set to 0.1 in the beginning but is multiplied or divided by 5 depending on whether the convergence ratio (χ_{k+1}^2/χ_k^2) falls below 0.25 or exceeds 1.1. After 100 iterations, the procedure eventually yields $n_e = 517.0 \text{ cm}^{-3}$, $T_c = 27.0 \text{ eV}$, $n_h/n_c = 0.02$, and $T_h/T_c = 2.44$. These values are in good agreement with the results shown in the top-left panel of Figure 2 in M22, despite that in M22, the observed QTN spectrum in a wider frequency range was fitted to a synthetic QTN spectrum including contributions from the electrons, protons, impact noise, galaxy radiation, and instrument noise.

The LM method described above is sensitive to the initial parameter guesses used. For the example QTN spectrum shown in Figure 1, the black, blue, and red dots in Figures 2(a) and (b) display, respectively, how n_e and T_c vary with the number of iteration steps when different initial values are used in the LM method. The three sets of initial parameter values tested are $(n_e, T_c, n_h/n_c, T_h/T_c) = (600.0 \text{ cm}^{-3}, 40.0 \text{ eV}, 0.05, 2.00)$, $(600.0 \text{ cm}^{-3}, 40.0 \text{ eV}, 0.02, 2.44)$, and $(500.0 \text{ cm}^{-3}, 20.0 \text{ eV}$,

$0.05, 2.00)$, as listed in the legend of Figure 2(b). The calculated n_e values after 100 iterations are 448.3, 460.6, and 498.3 cm^{-3} , respectively. For comparison, the horizontal dashed line in Figure 2(a) marks the “true” value of $n_e = 517.0 \text{ cm}^{-3}$ which is obtained with the carefully selected initial parameter values as discussed above. Clearly, the n_e values calculated in the LM method for different initial parameter values are quite different. Similarly, Figure 2(b) demonstrates that the T_c values obtained also vary with the initial parameter values. In comparison with the “true” value of $T_c = 27.0 \text{ eV}$ denoted by the horizontal dashed line, the calculated T_c values after 100 iterations are 29.7, 30.5, and 26.8 eV for the three test sets of initial parameters, respectively. On the other hand, it should be mentioned that the values of n_h/n_c and T_h/T_c have been fixed during the iterations shown in Figure 2 for simplicity. This is because our test calculations (not shown) have shown that the theoretical electron QTN spectrum is not sensitive to the values of n_h/n_c and T_h/T_c . This is indeed confirmed by the results indicated by the black and

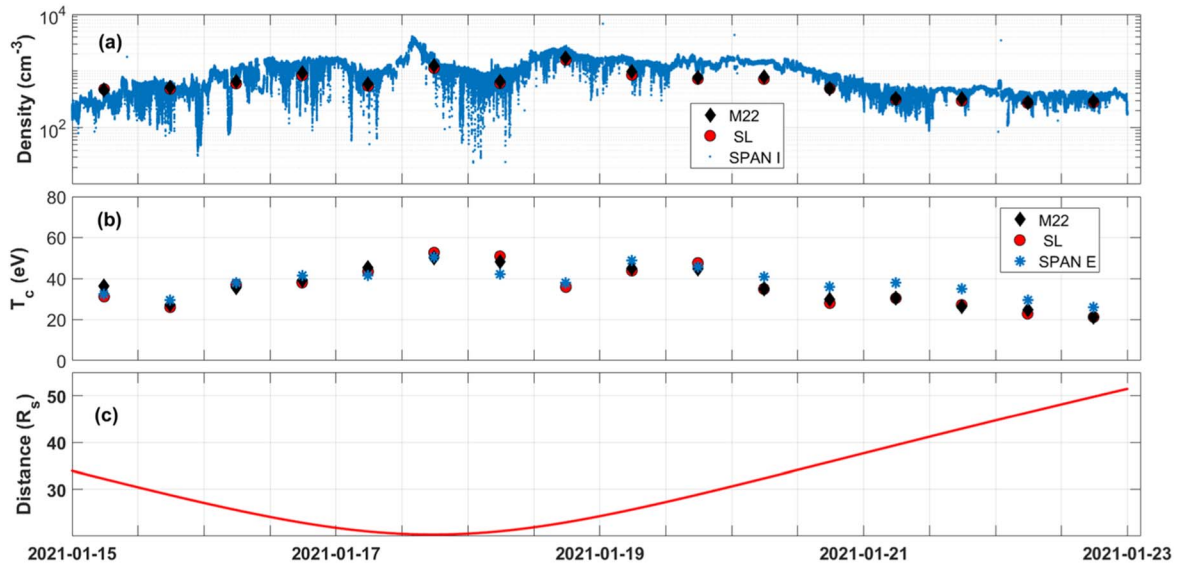


Figure 3. Comparison of (a) the electron density and (b) core temperature calculated using the new SL method (red dots) and the LM method in M22 (black diamonds) for PSP Encounter 7. The proton density obtained from SPAN-I measurements and the electron core temperature from SPAN-E data are shown as blue dots in (a) and (b), respectively. (c) The radial distance of PSP from the Sun.

blue dots being close to each other in Figures 2(a) and (b). The two corresponding sets of initial parameters have the same n_e and T_c values but different values of n_h/n_c and T_h/T_c .

To overcome the limitation of the LM method being sensitive to initial guess values, the present study combines the SD and LM algorithms to construct a new fitting approach (named the SL method), which is more flexible to initial parameter guesses. As the SD algorithm often provides a slow but certain convergence to a local minimum, the new fitting approach first employs the SD algorithm with a generic initial parameter set $(n_e, T_c, n_h/n_c, T_h/T_c) = (600.0 \text{ cm}^{-3}, 40.0 \text{ eV}, 0.05, 2.00)$. The step size factor α in the SD iterations is set to 0.01 after lots of tests (with α varying from 0.001 to 1). The SD iterations would be stopped when the convergence ratio consecutively exceeds 1 twice. Subsequently, the LM method, as described above, takes over with the parameter values yielded by the SD iterations as initial values. The LM iterations are finally terminated when the total iteration number (including the preceding SD iterations) reaches 100. The gray empty circles and solid dots in Figure 2 display the results from the combined SL method using the generic initial parameter combination. The variations of n_e and T_c with the iteration number are shown in Figures 2(a) and (b), respectively. There are 19 SD iterations and 81 LM iterations. The results given by the early SD iterations are shown as empty circles to be distinguished from the values yielded by the subsequent LM iterations (solid dots). The procedure eventually produces $n_e = 515.1 \text{ cm}^{-3}$ and $T_c = 26.9 \text{ eV}$. Clearly, the combined SL approach yields more accurate n_e and T_c than the LM method (see the black dots in Figure 2), with the generic initial parameter values. In addition, the results from the SL method using the initial parameter set of $(n_e, T_c, n_h/n_c, T_h/T_c) = (500.0 \text{ cm}^{-3}, 20.0 \text{ eV}, 0.05, 2.00)$ are shown as the magenta empty circles and solid dots in Figure 2. As the gray ones, the magenta empty circles and solid dots denote the values yielded by the early SD and late LM iterations, respectively. Compared with the LM method results (the black and red dots in Figure 2), the results from the new SL approach

Table 1
Initial Parameter Values Used in the LM Method of M22

Time	n_e	T_c	n_h/n_c	T_h/T_c
2021-01-15 05:50 ~ 51	402.63	30.72	0.02	1.90
2021-01-15 17:50 ~ 51	584.03	30.29	0.01	2.10
2021-01-16 05:50 ~ 51	896.47	40.37	0.005	6.00
2021-01-16 17:50 ~ 51	897.57	42.43	0.02	1.90
2021-01-17 05:50 ~ 51	596.69	44.46	0.02	2.00
2021-01-17 17:50 ~ 51	1337.55	50.04	0.005	2.00
2021-01-18 05:50 ~ 51	697.91	41.85	0.02	4.00
2021-01-18 17:50 ~ 51	1699.54	37.17	0.02	1.90
2021-01-19 05:50 ~ 51	1066.82	48.36	0.02	1.50
2021-01-19 17:50 ~ 51	881.81	49.47	0.04	1.90
2021-01-20 05:50 ~ 51	983.89	41.03	0.02	2.10
2021-01-20 17:50 ~ 51	673.13	35.04	0.25	2.40
2021-01-21 05:50 ~ 51	424.75	37.16	0.25	1.40
2021-01-21 17:50 ~ 51	456.04	34.63	0.025	1.40
2021-01-22 05:50 ~ 51	358.18	29.19	0.04	2.10
2021-01-22 17:50 ~ 51	387.21	26.34	0.01	2.10

with the different sets of initial parameters are closer to each other, indicating that the SL approach is less sensitive to the initial values used.

4. Data Analysis

The new SL method described in Section 3 is applied to analyze the PSP QTN spectra with the generic initial parameter set $(n_e, T_c, n_h/n_c, T_h/T_c) = (600.0 \text{ cm}^{-3}, 40.0 \text{ eV}, 0.05, 2.00)$. As aforementioned, the theoretical electron QTN spectrum is not sensitive to the values of n_h/n_c and T_h/T_c , so their values have been fixed during the iterations to save computation time. The calculated n_e and T_c during the antenna-unbiased intervals of Encounter 7 are shown as the red dots in Figures 3(a) and (b), respectively. In comparison, the n_e and T_c values given by the LM method in M22 are displayed as black diamonds. These values were obtained using specific initial parameter values as listed in Table 1. In addition, the blue dots further present the

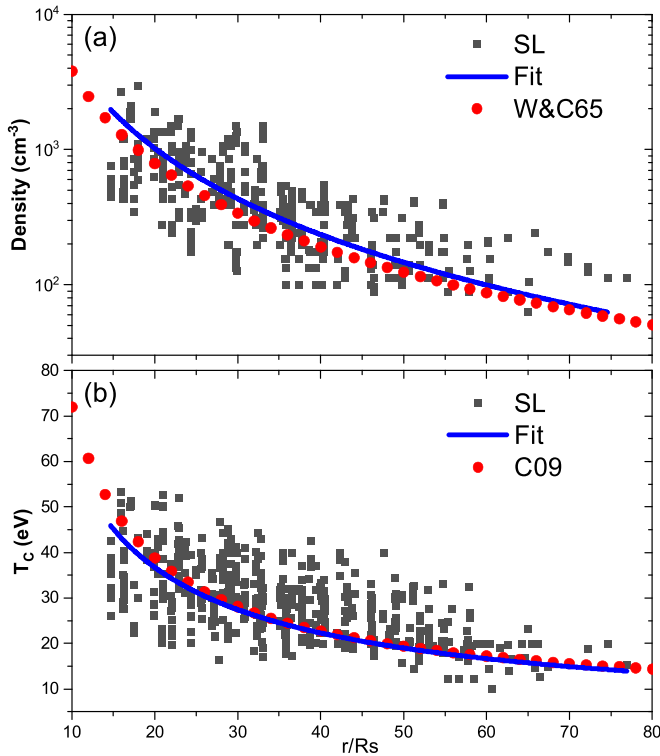


Figure 4. (a) Electron density and (b) core temperature as a function of the radial distance from the Sun. In each panel, the black squares are the values of the corresponding electron parameter calculated using the new SL method from the PSP QTN spectra of 10 encounters, the blue curve represents their power-law fit, and the red dots are from a theoretical or empirical solar wind model as described in the text.

proton density from the Solar Probe Analyzer for Ions (SPAN-I; Kasper et al. 2016) in Figure 3(a) and the core electron temperature from the Solar Probe Analyzer for Electrons (SPAN-E; Whittlesey et al. 2020) in Figure 3(b). Besides the general consistency between the M22 results and the measurements of SPAN-I and SPAN-E (which has already been demonstrated in Figure 3 of M22), Figures 3(a) and (b) here show nice agreement between the results calculated using the new SL method and those in M22. This demonstrates that the new SL method is fairly reliable, even with the generic initial parameter values. Finally, Figure 3(c) presents the radial distance of PSP from the Sun. The perihelion is at $\sim 20 R_s$ during Encounter 7. Figures 3(a)–(c) together suggest that both the electron density and core temperature tend to increase as the radial distance decreases, consistent with the findings in Maksimovic et al. (2020).

To further examine how n_e and T_c vary with the radial distance from the Sun (r), the n_e and T_c values calculated using the SL method (with the generic initial parameter values) during the antenna-unbiased intervals of 10 encounters (Encounters 3 to 13, except Encounter 11) are presented in Figures 4(a) and (b) as a function of r . As mentioned in Section 2, the present study deals with the 1 minute median data. There are 744 data points in total during the 10 encounters analyzed. They encompass a radial distance range between 12 and $80 R_s$. Statistically, both n_e and T_c decrease with increasing r . The power-law fitting of the calculated electron parameter values yields $n_e = n_0 r^{-2.12 \pm 0.03}$ with $n_0 = (6.20 \pm 0.01) \times 10^5 \text{ cm}^{-3}$ and $T_c = T_0 r^{-(0.71 \pm 0.03)}$ with $T_0 = (3.2 \pm 0.2) \times 10^2 \text{ eV}$. They are shown as the blue curves in Figures 4(a) and (b), respectively. In addition, the red dots in

Figure 4(a) are from the theoretical solar-wind model of Whang & Chang (1965). They are in good agreement with the blue curve. On the other hand, the red dots in Figure 4(b) represent the empirical model results of Cranmer et al. (2009) based on the Helios and Ulysses plasma instrument data between 0.29 and 5.4 au. They also follow the blue curve closely. Note that Moncuquet et al. (2020) derived from the PSP QTN spectral measurements during Encounters 1 and 2 that $T_e \propto r^{-0.74 \pm 0.03}$. Also, the statistical studies of Maksimovic et al. (2020), Maksimovic et al. (2000) suggested that $T_e \propto r^{-0.6 \sim -0.8}$. All of these results are consistent with the power-law fit for T_c in Figure 4(b). In contrast, Štverák et al. (2015) concluded from Helios data between 0.3 and 1 au that $T_e \propto r^{-0.59}$ for slow solar wind and $T_e \propto r^{-0.31}$ for fast solar wind, respectively. The discrepancies could be attributed to several factors, such as the different solar conditions when measurements were made, the different radial distance ranges of the measurements, and the impact of nonlocal heating and heat transfer on the electron temperature, even in the presence of the same solar-wind stream.

5. Conclusions

The present study combines the SD and LM algorithms to construct an improved method to fit the PSP QTN measurements to calculate the solar wind electron density and core temperature. Compared with the traditional LM method, the new SL method is more flexible with initial guess values and yields reliable solar wind electron density and temperature with a generic set of initial parameter values. The fitting is focused on the observed QTN spectra in the frequency range of $0.9\text{--}5f_p$, where the electron QTN dominates the QTN contributions from other sources. Subsequently, the observed QTN spectra are directly fitted to the theoretical electron QTN with the ARF given in M22. In addition, for simplicity, the fitting has been performed with the values of n_h/n_c and T_h/T_c fixed during iterations, because our calculations demonstrate that the results are not sensitive to these two parameters.




The new SL fitting approach has been applied to analyze the PSP QTN measurements during the antenna-unbiased intervals of 10 encounters (Encounters 3 to 13, except Encounter 11). The analysis gives the solar wind electron density and core temperature between 12 and $80 R_s$ of heliocentric distance. The results indicate that $n_e \propto r^{-2.12}$ and $T_e \propto r^{-0.71}$, in agreement with existing models and previous results. On the other hand, the theoretical electron QTN model adopted in the present study assumes that the solar wind electrons consist of a thermal core and a suprathermal halo following isotropic Maxwellian distributions. This is certainly not a realistic representation of the solar wind electrons. How to better model the solar wind electron QTN spectrum and, more importantly, expand the QTN analysis to the PSP antenna-biased intervals remains an important task for future research.

Acknowledgments

This work was supported by the Strategic Priority Research Program of the Chinese Academy of Sciences (grant XDB 41000000), the National Natural Science Foundation of China (NSFC) grant 42174203, the Guangdong Pearl River Talent Program (2019QN01G838), and Shenzhen Science and Technology Program (grant JCYJ20210324104810027). V.P. acknowledges the project 21GRD02 BIOSPHERE from the European Partnership on Metrology, cofinanced by the

European Union's Horizon Europe Research and Innovation Programme and by the participating states. We also thank the PSP mission for the use of FIELDS and SPAN data in this study.

ORCID iDs

Xianming Zheng  <https://orcid.org/0009-0005-7089-9749>
 Kaijun Liu  <https://orcid.org/0000-0001-5882-1328>
 Mihailo M. Martinović  <https://orcid.org/0000-0002-7365-0472>
 Viviane Pierrard  <https://orcid.org/0000-0001-5014-7682>
 Mingzhe Liu  <https://orcid.org/0000-0003-2981-0544>
 Qingbao He  <https://orcid.org/0000-0003-2605-7083>
 Kun Cheng  <https://orcid.org/0000-0003-1019-2598>
 Yan Wang  <https://orcid.org/0000-0001-6783-7591>

References

- Aster, R. C., Borchers, B., & Thurber, C. H. 2018, *Parameter Estimation and Inverse Problems* (Amsterdam: Elsevier)
- Bale, S. D., Badman, S. T., Bonnell, J. W., et al. 2019, *Natur*, **576**, 237
- Bale, S. D., Goetz, K., Harvey, P. R., et al. 2016, *SSRv*, **204**, 49
- Couturier, P., Hoang, S., Meyer-Vernet, N., & Steinberg, J.-L. 1981, *JGRA*, **86**, 11127
- Cranmer, S. R., Matthaeus, W. H., Breech, B. A., & Kasper, J. C. 2009, *ApJ*, **702**, 1604
- Fejer, J., & Kan, J. 1969, *RaSc*, **4**, 721
- Fox, N. J., Velli, M. C., Bale, S. D., et al. 2016, *SSRv*, **204**, 7
- Gurnett, D. 1998, *GMS*, **103**, 121
- Issautier, K., Meyer-Vernet, N., Moncuquet, M., & Hoang, S. 1996, *GeoRL*, **23**, 1649
- Issautier, K., Meyer-Vernet, N., Moncuquet, M., Hoang, S., & McComas, D. 1999, *JGRA*, **104**, 6691
- Issautier, K., Perche, C., Hoang, S., et al. 2005, *AdSpR*, **35**, 2141
- Knoll, R., Epstein, G., Hoang, S., et al. 1978, *IEEE*, **16**, 199
- Liu, M., Issautier, K., Meyer-Vernet, N., et al. 2021, *A&A*, **650**, A14
- Liu, M., Issautier, K., Moncuquet, M., et al. 2023, *A&A*, **674**, A49
- Kasper, J. C., Abiad, R., Austin, G., et al. 2016, *SSRv*, **204**, 131
- Maksimovic, M., Bale, S. D., Berčič, L., et al. 2020, *ApJS*, **246**, 62
- Maksimovic, M., Bougeret, J. L., Perche, C., et al. 1998, *GeoRL*, **25**, 1265
- Maksimovic, M., Gary, S. P., & Skoug, R. M. 2000, *JGRA*, **105**, 18337
- Maksimovic, M., Hoang, S., Meyer-Vernet, N., et al. 1995, *JGRA*, **100**, 19881
- Martinović, M., Zaslavsky, A., Maksimović, M., et al. 2016, *JGRA*, **121**, 129
- Martinović, M., Zaslavsky, A., Maksimović, M., & Issautier, K. 2017, *POBeo*, **96**, 141
- Martinović, M. M., Klein, K. G., & Krishnan, H. G. 2022, *RNAAS*, **6**, 166
- Martinović, M. M., Kristopher, G. K., Savannah, R. G., et al. 2020, *JGRA*, **125**, e2020JA028113
- Meyer-Vernet, N. 1979, *JGRA*, **84**, 5373
- Meyer-Vernet, N., Issautier, K., & Moncuquet, M. 2017, *JGRA*, **122**, 7925
- Meyer-Vernet, N., & Perche, C. 1989, *JGRA*, **94**, 2405
- Moncuquet, M., Lecacheux, A., Meyer-Vernet, N., Cecconi, B., & Kurth, W. S. 2005, *GeoRL*, **32**, L20S02
- Moncuquet, M., Meyer-Vernet, N., Issautier, K., et al. 2020, *ApJS*, **246**, 44
- Pulupa, M., Bale, S. D., Bonnell, J. W., et al. 2017, *JGRA*, **122**, 2836
- Štverák, Š., Trávníček, P. M., & Hellinger, P. 2015, *JGRA*, **120**, 8177
- Whang, Y. C., & Chang, C. C. 1965, *JGR*, **70**, 4175
- Whittlesey, P. L., Larson, D. E., Kasper, J. C., et al. 2020, *ApJS*, **246**, 74
- Zouganelis, I., Maksimovic, M., Meyer-Vernet, N., et al. 2010, *RaSc*, **45**, 1005